J. Fluid Mech. (2020), *vol.* 889, A23. © The Author(s), 2020.
Published by Cambridge University Press
doi:10.1017/jfm.2020.87

The effect of a strong density step on blocked stratified flow over topography

Arjun Jagannathan[1],†, **Kraig B. Winters**[1] **and Laurence Armi**[1]

[1]Scripps Institution of Oceanography, University of California San Diego, La Jolla, CA 92093, USA

(Received 21 May 2019; revised 22 January 2020; accepted 24 January 2020)

The dynamical connection between topographic control and wave excitation aloft is investigated theoretically and numerically in the idealized setting of two-dimensional stratified flow over an isolated ridge. We consider a constant far upstream inflow with uniform stratification except for a sharp density step located above the height of the ridge crest. Below this step, the stratification is sufficiently strong that the low level flow is blocked upstream and a hydraulically controlled flow spills over the crest. Above the density step, the flow supports upward radiating waves. In the inviscid limit, a bifurcating isopycnal separates the hydraulically controlled overflow from the wave field aloft. We show that, depending on the height of the density step, the sharp interface can either remain approximately flat, above the controlled downslope flow, or plunge in the lee of the obstacle as part of the controlled overflow itself. Whether the interface plunges or not is a direct consequence of hydraulic control at the crest. The flow above the crest responds to the top of the sharp density step as if it were a virtual topography. We find that a plunging interface can excite a wave field aloft that is approximately six times as energetic, with 15 % higher pressure drag, than that in a comparable flow in which the interface remains approximately flat.

Key words: hydraulic control, topographic effects, stratified flows

1. Introduction

There is a considerable body of literature (cf. Long 1955; Pierrehumbert & Wyman 1985; Baines 1987) on the phenomenon of upstream blocking, which occurs whenever the height h_m of an obstacle in a stratified flow is greater than the energetic vertical excursion scale V_∞/N_0. Here V_∞ and N_0 are, respectively, the background flow speed and buoyancy frequency, assumed constant. An obstacle that exerts upstream influence, leading to flow deceleration and blocking, is referred to as dynamically tall. To preserve continuity, the fluid immediately overlying the upstream blocked layer accelerates and plunges asymmetrically across the crest as a hydraulically controlled overflow (Baines & Hoinka 1985). The top of this asymmetric overflow is marked by a bifurcating isopycnal which partially separates it from the overlying flow. While this bifurcating isopycnal and the resultant isolating layer (Smith 1985; Winters & Armi 2014) dynamically insulate the topographically controlled overflow

† Email address for correspondence: ajagannathan@atmos.ucla.edu

from the surrounding flow, the flow field aloft can be influenced by the shape and character of the overflow. The dynamical connection between hydraulic control and the flow structure further aloft has been a subject of interest ever since the pioneering theoretical and experimental studies of Long (1955).

Hydraulically controlled flows that include density steps occur both in the ocean and the atmosphere. In their observations of the overflow in the Panay Sill, Tessler *et al.* (2010) noted the presence of a sharp density interface in the subthermocline water that plunges across the sill. Recently, Armi & Mayr (2015) described the observation of a hydraulically controlled flow in the Sierras in which a nearly neutral lower layer capped by a strong density step overflows asymmetrically across the mountain crest. Their observations showed that the density step at the top of the controlled overflowing layer forms a 'virtual topography' so that the flow aloft responds to the shape of the density step across the crest rather than the real topography underneath. Motivated by these observations, here we numerically explore 'virtual topography' effects in blocked stratified flows where a strong density step is present above the crest level. A theoretical framework to interpret the flow solutions is also presented.

Jagannathan, Winters & Armi (2019) investigated flow splitting effects in stratified flows encountering dynamically tall, long mountain ridges. In these flows, the fluid below a depth δ from the crest remains stagnant or flows around the sides of the ridge. Above this blocked fluid is a plunging, asymmetric overflow that is hydraulically controlled at the crest. A schematic of this flow in a purely two-dimensional (2-D) setting is shown in figure 1(*a*). For a given obstacle height h_m, upstream flow speed V_∞ and stratification N_0, the important non-dimensional parameter is $V_\infty/(N_0 h_m)$. The inverse quantity $h_m/(V_\infty/N_0)$ is sometimes referred to as a dimensionless obstacle height (e.g. Epifanio & Durran 2001), while other authors (e.g. Miles & Huppert 1969; Baines 1998) leave this dimensionless group nameless. The identification of $V_\infty/(N_0 h_m)$ as a Froude number is common in the literature (e.g. Brighton 1978; Smolarkiewicz & Rotunno 1989; Hunt *et al.* 1997; Legg & Klymak 2008; Pal *et al.* 2017). For consistency with our previous work, we denote $V_\infty/(N_0 h_m) = Fr$, where Fr is a bulk parameter relating far upstream flow properties with the obstacle height. In blocked flows, Fr may be approximately thought of as the ratio of the background flow speed and the propagation speed $N_0 h_m/\pi$ of a columnar internal wave mode that accomplishes upstream blocking. Note that Fr should not be confused with the dynamic or inner Froude number that relates the flow speed and long wave speed within the streamtube overflowing the crest.

Winters & Armi (2014) showed that when blocking effects are significant, or equivalently, when $Fr \ll 1$, the optimally controlled overflow has a parabolic velocity profile upstream of the blocking location, with the layer thickness H and volume transport Q coupled through the control relationship $Q = N_0 H^2/\pi$. The height of the bifurcating isopycnal of this optimally controlled flow is then given by $z = z_{op} = h_m - \delta + H$. For a given upstream flow configuration, H can be determined by solving a kinematic equation for the overflow transport (e.g. Winters & Armi 2014; Jagannathan *et al.* 2019). These predictions were corroborated in Jagannathan *et al.* (2019), where it was also noted that, contrary to the Winters & Armi (2014) assumption, the flow above the bifurcating isopycnal is not completely dynamically uncoupled from the controlled flow beneath. Rather, the asymmetric plunging overflow acts like a virtual topography for the flow aloft in a manner similar to that described by Armi & Mayr (2015) (cf. figure 3 of their paper), launching vertically propagating internal waves of wavelength approximately $2\pi V_\infty/N_0$.

Winters & Armi (2012, 2014) studied blocking and hydraulic dynamics in low Fr, uniformly stratified flow over an infinite obstacle, but did not consider the effects

of non-uniform stratification, e.g. density steps. Here we investigate blocked flows which feature a strong density step embedded within an otherwise uniformly stratified fluid. This flow configuration is shown schematically in figure 1(*b*). A density step of magnitude $\Delta\rho_i$ is located at $z = z_0$ such that $h_m < z_0 < z_{op}$. That is, the step is above crest level but below the height of the bifurcating isopycnal in the corresponding uniformly stratified case. The thickness of the interface is assumed to be small but finite, that is $\delta_i/H \ll 1$, so that the stratification changes abruptly, $N_{\delta_i}/N_0 \gg 1$, where N_{δ_i} and N_0 are the stratification within and away from the interface, respectively. This flow configuration is comparable to the observed stratification and velocity profiles at the Panay Sill by Tessler *et al.* (2010) (e.g. figures 2 and 3 of their paper) where the ratio of the stratification within the density interface and the layer below is approximately 5 and the flow also appears to be approximately motionless upstream of the crest.

We will show that the spatial location of the density step relative to h_m and z_{op} strongly influences the height of the bifurcating isopycnal. Further we will also demonstrate that the amplitude of the mountain wave aloft is directly connected to the nature of the hydraulically controlled overflow and in particular depends sensitively on whether or not the density interface is drawn down asymmetrically across the crest as part of the plunging overflow.

2. Model description

The governing equations are the two-dimensional, non-rotating equations of motion for a stratified fluid in the Boussinesq limit. The numerical model used for the computations is the spectral solver flow_solve described in Winters & De la Fuente (2012), with hyper-viscosity to dissipate subgrid scale motions. We consider a background state characterized by a far upstream flow speed V_∞ and stratification $N(z)$ incident on a Gaussian topography

$$h = h_m \exp(-y^2/\sigma_y^2); \quad h_m/\sigma_y = 1/6. \tag{2.1a,b}$$

The topography is centred in a domain of width $L_y = 33\sigma_y$ and is incorporated via the immersed boundary set-up discussed in Winters & De la Fuente (2012), with conditions of free-slip at the obstacle surface. While the obstacle is gently sloping ($h_m/\sigma_y = 1/6$), the numerical model itself is non-hydrostatic. The height of the computational domain is $L_z = 6h_m$ and the density profiles considered are as shown in figure 1(*b*). In the computations, the density step $\Delta\rho_i$ over a height δ_i is represented using a hyperbolic tangent function as

$$\begin{aligned}\rho \;=\; & \rho_0 + 0.5\Delta\rho_2 \left(\frac{L_z - z}{L_z - z_0}\right)\left[1 + \tanh\left(\frac{2(z - z_0 - \delta_i/2)}{\delta_i}\right)\right] \\ & + 0.5\left(\Delta\rho_2 + \Delta\rho_i + \left(\frac{z_0 - z}{z_0}\right)\Delta\rho_1\right)\left[1 - \tanh\left(\frac{2(z - z_0 - \delta_i/2)}{\delta_i}\right)\right],\end{aligned} \tag{2.2}$$

so that the bottom of the step is located at $z = z_0$. The corresponding stratification profiles are then approximately given by

$$N(z) \approx \begin{cases} N_{\delta_i}; & |z - z_0 - \delta_i/2| \leqslant \delta_i/2, \\ N_0; & |z - z_0 - \delta_i/2| > \delta_i/2. \end{cases} \tag{2.3}$$

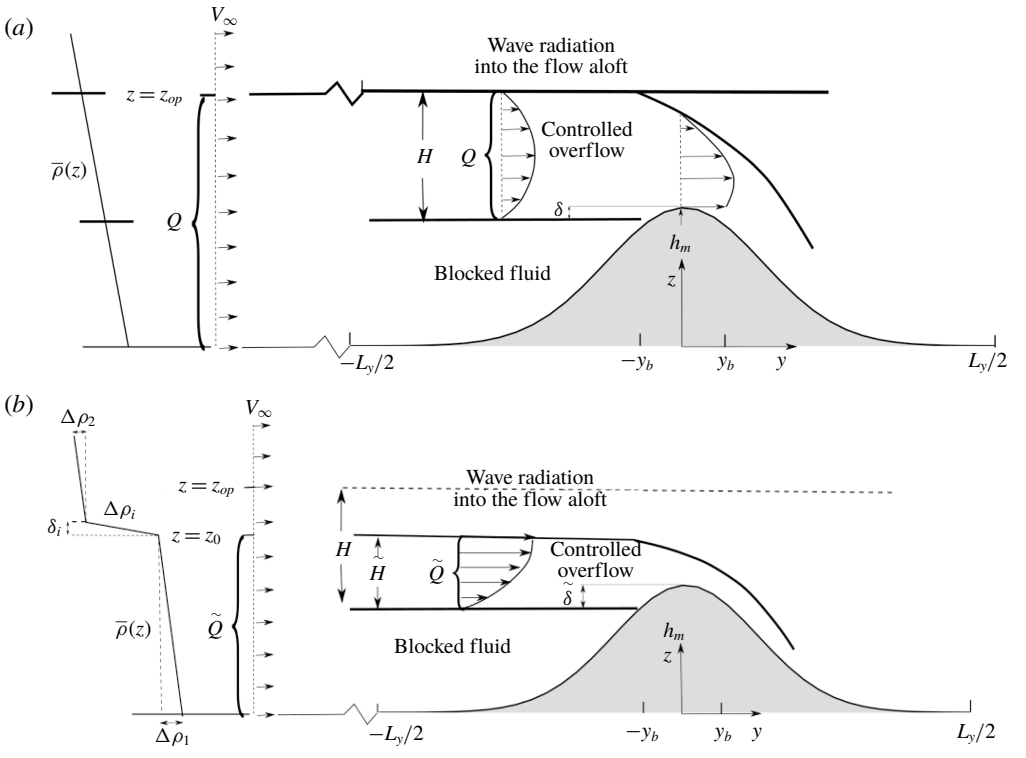

FIGURE 1. (*a*) Schematic of low Fr controlled asymmetric overflow over an infinite ridge for the case of uniform upstream stratification and flow speed. The upstream fluid below a depth δ from the crest is blocked. The streamwise coordinate of the blocking location is $y = -y_b$, and Q denotes the volume transport within the overflow, which matches the far upstream transport as shown. The streamwise computational boundaries are $y = -L_y/2$ and $y = L_y/2$. The optimally controlled overflow has a parabolic velocity profile, with the height of the bifurcating isopycnal being $z = z_{op}$. Panel (*b*) is as in figure 1(*a*) but for the case when a density step is present in an otherwise uniformly stratified fluid with $Fr = V_\infty/N_0 h_m \ll 1$. The density step $\Delta\rho_i$ is large and the interface is thin relative to H ($\delta_i/H \ll 1$), so that $N_{\delta_i}/N_0 \gg 1$, where N_{δ_i} and N_0 denote the stratification within and away from the interface, respectively. The flow arrows indicate that the far upstream inflow speed is a constant V_∞ up to an arbitrary height $z > z_{op}$. For $z = z_0 < z_{op}$, the upstream thickness of the overflow is $\widetilde{H} < H$ and the velocity profile deviates from the optimal parabolic shape as indicated. Note that the downward arrows associated with H and $\widetilde{H}$ point to different z locations. This is in anticipation of the result (see also, § 3) that the blocking scale $\widetilde{\delta}$ when the isopycnal bifurcates at the vertical level of the density step is different from the blocking scale δ when no density step is present.

We fix $Fr = 0.16$ and consider strong density steps characterized by the dimensional values $N_0 = 10^{-2}\,\mathrm{s}^{-1}$ and $N_{\delta_i} = 8.6N_0 = 8.6 \times 10^{-2}\,\mathrm{s}^{-1}$. In Jagannathan *et al.* (2019), we showed that for a blocking scale $\widetilde{\delta}$, the appropriate inner horizontal length scale for the overflow is the half-width of the obstacle at the blocking level $\sigma_{y_{\widetilde{\delta}}}$. The smallest vertical length scale is the thickness of the density interface δ_i which, in our experiments,

is much smaller than the blocking scale $\widetilde{\delta}$. To resolve these inner length scales, we choose a grid spacing $\Delta z \approx \delta_i/6$ and $\Delta y \approx \sigma_{y_{\widetilde{\delta}}}/10$.

A sponge layer of thickness $L_z/4$ is placed at the upper boundary to prevent reflection of vertically propagating waves and the upstream boundary condition evolves slowly through an iterative scheme (Jagannathan *et al.* 2019) that accounts for upstream influence of the topography. Arrest of the forward energy cascade due to downstream instabilities and overturns is accomplished by sixth-order hyperviscous and hyperdiffusion operators (Winters & De la Fuente 2012). The flow speed is rapidly accelerated from rest toward its target speed V_∞ over approximately ten time steps. We judge the flow to be quasi-steady when, at the blocking location just upstream of the crest, the peak speed in the overflow varies in time by less than 1 % of its mean value.

3. Numerical results

When $Fr \ll 1$, across-crest asymmetry induced by upstream blocking forces a flow response that is characterized by hydraulic control at the crest (cf. Winters 2016; Jagannathan *et al.* 2019). For the uniformly stratified case depicted in figure 1(*a*), Winters & Armi (2014) show that the upstream flow has a parabolic shape above the blocking level, with peak speed given by $1.5N_0H/\pi$. Further, the blocking scale is also related to the overflow thickness as $\delta = H/8$. The statement of volume flux conservation for the overflow then reads (see also Jagannathan *et al.* (2019))

$$N_0H^2/\pi = V_\infty(h_m + 7H/8). \tag{3.1}$$

The unknown thickness H is obtained as the positive root of this equation:

$$H = \frac{\dfrac{7\pi V_\infty}{8N_0} + \sqrt{\left(\dfrac{7\pi V_\infty}{8N_0}\right)^2 + \dfrac{4\pi V_\infty h_m}{N_0}}}{2}. \tag{3.2}$$

Note that H can also be written in terms of h_m and Fr as

$$H = \frac{\dfrac{7\pi}{8}h_mFr + h_m\sqrt{\left(\dfrac{7\pi}{8}\right)^2 Fr^2 + 4\pi Fr}}{2}. \tag{3.3}$$

Thus for a fixed Fr, the overflow thickness H is directly proportional to h_m.

Keeping the other parameters same, we now consider the effect of including a strong density step within the stratification profile. In the simulations that follow, we set $Fr = 0.16$ and the ratio N_{δ_i}/N_0 to 8.6. Substituting $Fr = 0.16$ in (3.2) yields $H = 0.96h_m$. That is, the bifurcating isopycnal for a uniformly stratified flow at this Fr will be at $z_{op} = h_m + (7/8)0.96h_m = 1.84h_m$. When the step is placed at $z_0 > z_{op}$, we expect to recover the Winters & Armi (2014) solution, depicted schematically in figure 1(*a*).

As an example, consider a strong density interface located well above z_{op}, at $z_0 = 2.23h_m$. Contours of isopycnals and streamwise velocity of the quasi-steady flow for this case (figure 2) reveal that the overflow bifurcates at $z \approx z_{op}$ and not $z = z_0$. The vertical profile of the overflow at the upstream blocking location (figure 3) also agrees closely with the parabolic prediction of Winters & Armi (2014). We also note

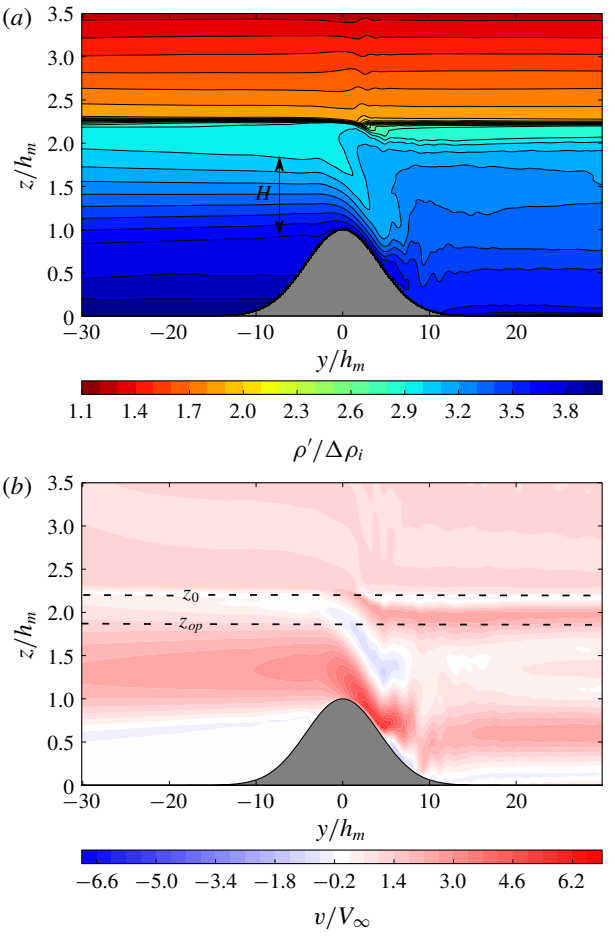

FIGURE 2. Quasi-steady flow field for 2-D $Fr = 0.16$ flow over an infinite ridge with a density step characterized by $N_{\delta_i}/N_0 = 8.6$ located at $z_0 = 2.23h_m$. (*a*) Isopycnal lines and contours and (*b*) streamwise velocity contours. Flow is from left to right.

that the presence of the density step above the bifurcation acts to strongly inhibit isopycnal displacements aloft. This is similar to observations above the Panay Sill by Tessler *et al.* (2010) (e.g. figure 4 of their paper), where the sub-thermocline overflow plunges down the lee slope, but isopycnal displacements above the strongly stratified thermocline are suppressed.

We now present results from two numerical simulations which highlight by comparison the strong coupling between hydraulic control of the overflow and wave excitation aloft. These simulations differ only in the vertical location of the density step, which is now in the height range $h_m < z_0 < z_{op}$, with Fr and N_{δ_i}/N_0 again being set to 0.16 and 8.6, respectively. In the first, we consider a case with the density interface at $z_0 = 1.73h_m$. We then lower the interface to $z_0 = 1.33h_m$. We will see that a topographically controlled overflow develops in both these flows, but that the flow morphology differs significantly. In particular, the density interface remains nearly flat in one case while it plunges across the crest in the other. We will see that whether the interface plunges with the overflow or not is determined by the fundamental

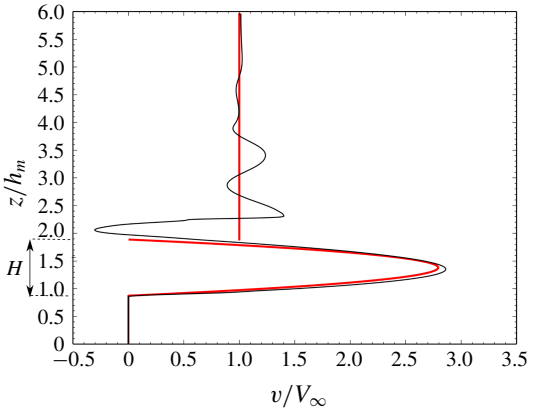

FIGURE 3. Vertical profile of the steady streamwise velocity at the blocking point $y=-y_b$ for $Fr=0.16$ flow over an infinite ridge with a sharp density step located at $z_0=2.23h_m$. The Winters & Armi (2014) parabolic overflow prediction is shown in red.

condition for crest control, namely that the upstream flow be subcritical to a long gravity wave mode.

The theoretical construct of a bifurcating isopycnal (Smith 1985; Winters & Armi 2014) as depicted in figure 1 has a well-defined bifurcation point, which is the upstream location where the lower branch of the bifurcating isopycnal begins to plunge. In numerical simulations, due to limitations of resolution and instability of the flow downstream (Smith 1991; Jagannathan, Winters & Armi 2017), the bifurcation manifests over a finite region above the blocking location rather than at a single point. This creates some ambiguity in identifying the bifurcating isopycnal. Here, we identify the topmost isopycnal below which the overflow accelerates and plunges across the crest as the bifurcating isopycnal. We will also show by solving the Taylor–Goldstein equation that this is precisely the lowest isopycnal that renders the upstream flow beneath it and above the blocked layer subcritical.

The time averaged, quasi-steady flow field for the case $z_0 = 1.73h_m$ (figure 4) exhibits upstream blocking and across-crest asymmetry. An accelerating downslope flow forms beneath a wedge of nearly stagnant mixed fluid, identifiable as the isolating layer. An isopycnal bifurcation occurs just beneath the sharp interface, at $z = z_0$, leaving the bulk of the stratified interface above the accelerated layer upstream and above the isolating layer downstream. Directly above the crest, the top of the interface is displaced slightly upward. This appears to be related to the shear instability that develops just downstream of the bifurcation point (e.g. Peltier & Scinocca 1990; Jagannathan *et al.* 2017).

3.1. *Non-plunging interface: weak perturbations aloft*

The key feature of the flow is that the density interface remains dynamically inactive; that is, it does not plunge across the crest as part of the hydraulically controlled overflow. The flow aloft responds to an effective flat bottom formed by the density interface rather than the real topography below. As a result, only weak flow perturbations occur in this region. These perturbations are small-amplitude, upward-propagating waves excited by time dependent disturbances of the density step near the bifurcation region.

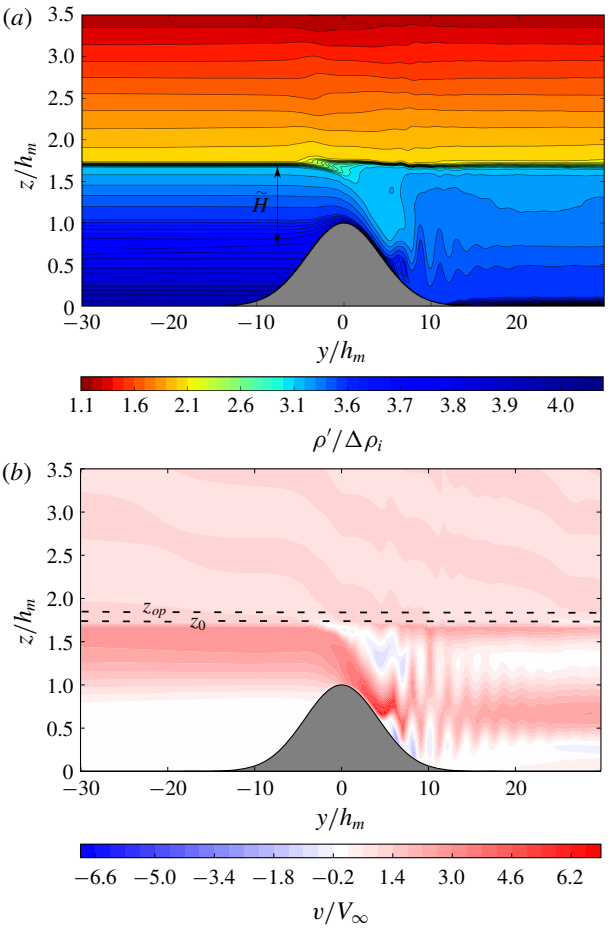

FIGURE 4. Same as figure 2 but for $z_0 = 1.73h_m$.

Figure 5 shows that the overflow profile at the upstream blocking location has a semi-parabolic shape rather than the parabolic shape observed when the stratification is uniform or when the density step is located above z_{op} as in figure 3. Recall that in the Winters & Armi (2014) solution, the blocking scale is dynamically related to the thickness of the parabolic overflow as $\delta = H/8$. Simulations over a range of small Fr suggest that when a strong density step is present at $z = z_0 < z_{op}$, the dynamical blocking scale is related to the thickness $\widetilde{H}$ of the semi-parabolic overflow as $\widetilde{\delta} \approx \widetilde{H}/4$.

The peak speed of the semi-parabolic overflow can be predicted as follows. The volume transport $\widetilde{Q}$ of the overflow must match the far upstream transport below the bifurcating isopycnal, which is simply given by $V_\infty z_0$ (see figure 1*b*). The peak speed v_m of the overflow at the blocking location is then obtained by solving the volume conservation equation

$$\widetilde{Q} = V_\infty z_0 = (2/3)\widetilde{H} v_m, \tag{3.4}$$

with $\widetilde{H} = z_0 - h_m + \widetilde{\delta} = z_0 - h_m + \widetilde{H}/4$, yielding

$$\widetilde{H} = \tfrac{4}{3}(z_0 - h_m). \tag{3.5}$$

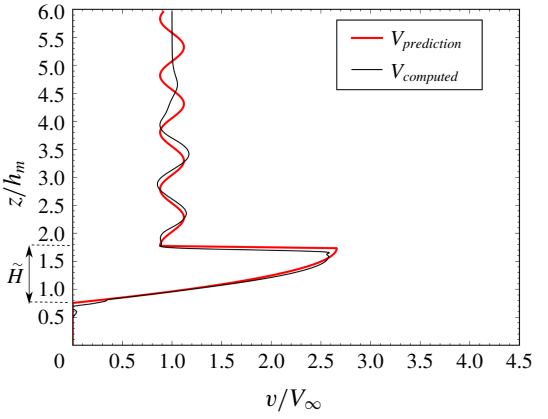

FIGURE 5. Vertical profile of the steady streamwise velocity at the blocking point $y=-y_b$ for $Fr=0.16$ flow over an infinite ridge with a sharp density step located at $z_0=1.73h_m$. The prediction in red is based on the values of $\widetilde{H}$ and v_m from (3.5) and (3.6), respectively. The wave aloft is predicted to have a vertical wavelength $2\pi V_\infty/N_0$ and perturbation speed amplitude $V_\infty N_0/N_{\delta_i}=0.12V_\infty$ (see § 6.1), with the phase chosen to match the computed solution.

Substituting (3.5) into (3.4), we obtain

$$v_m=\frac{9}{8}\frac{V_\infty z_0}{(z_0-h_m)}, \tag{3.6}$$

which furnishes a complete description of the overflow profile in terms of the known problem parameters V_∞, h_m and z_0.

Figure 5 shows that the peak speed of the overflow agrees well with the value obtained from (3.6). Within the density step, the flow speed decreases linearly to the ambient V_∞. Finally, above the step, small amplitude oscillations ($\approx 0.15V_\infty$) are present. These oscillations are characterized by nearly zero frequency and vertical wavelength identifiable as $2\pi V_\infty/N_0$, which is consistent with a vertically propagating linear mountain wave. Note that vertical propagation above $z\approx 4h_m$ is suppressed by the sponge layer.

3.2. *Plunging interface: large amplitude wave aloft*

When the density step is located closer to the crest, at $z=1.33h_m$, an asymmetric hydraulic response is again observed, but there are important differences with respect to the case $z_0=1.73h_m$. The isopycnals and streamwise velocity contours of the quasi-steady flow are shown in figure 6. Unlike in the previous case, the upstream flow now bifurcates at the top of the sharp interface, at $z=z_0+\delta_i$. The density step is thus a dynamically active component of the hydraulically controlled plunging overflow. It descends a depth of approximately $\widetilde{H}/2$ from its initial position, which is roughly $1.4V_\infty/N_0$ for the value $Fr=0.16$ considered.

The upstream velocity profile again has a semi-parabolic shape (figure 7). To predict its peak speed using a volume flux constraint, equation (3.4) must be modified to include the density step in the overflow. Once again assuming that the velocity

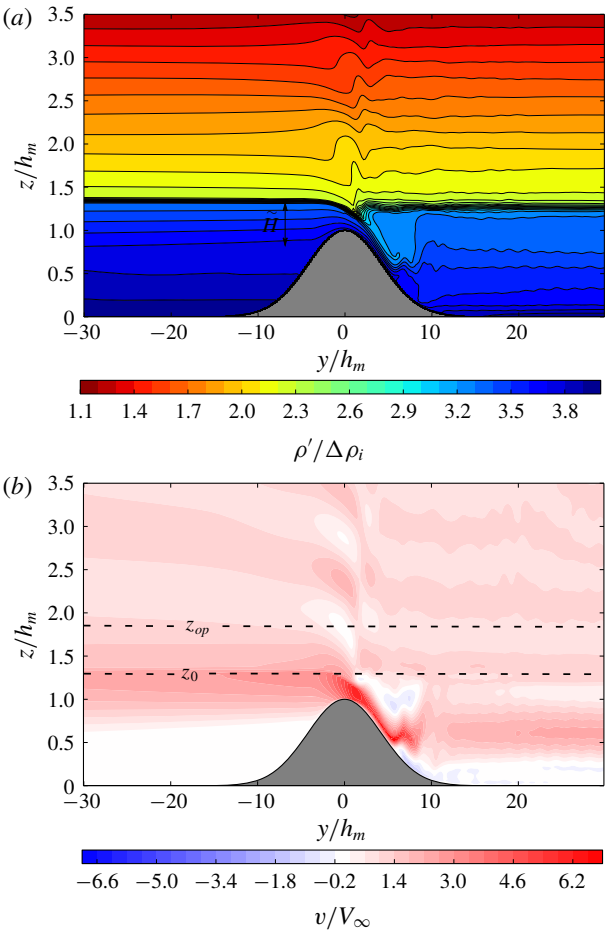

FIGURE 6. Same as figure 4 but for $z_0 = 1.33h_m$.

decreases linearly within the interface to the ambient V_∞, volume flux conservation requires that

$$\widetilde{Q} = V_\infty(z_0 + \delta_i) = (2/3)\widetilde{H}v_m + \frac{(v_m + V_\infty)}{2}\delta_i, \tag{3.7}$$

giving

$$v_m = \frac{V_\infty(z_0 + \delta_i/2)}{(2/3)\widetilde{H} + \delta_i/2}. \tag{3.8}$$

Figure 7 shows that the peak speed within the overflowing layer is now well estimated by (3.8). Further, the descending step acts as a virtual topography for the flow aloft and excites a large wave of amplitude approximately V_∞ rather than $0.15V_\infty$ as in the previous case. Interestingly, a comparison of figure 7 with figure 5 also reveals that there is a phase difference of approximately π in the vertical between the mountain wave in the present case and the small amplitude disturbance observed when the interface does not plunge. This is a consequence of the difference in the

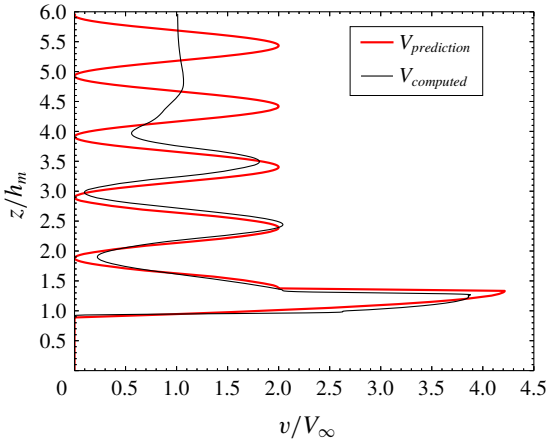

FIGURE 7. Same as figure 5 but for $z_0 = 1.33h_m$. The prediction for the peak speed is obtained from (3.8), while the wave aloft is assumed to have a vertical wavelength $2\pi V_\infty/N_0$ and perturbation speed amplitude of V_∞ (see § 6.1). The phase of the wave is chosen to match the computed solution.

shapes of the 'virtual topography' i.e. the top of the density step in these two flows – it descends sharply past the bifurcation point in one case while rising slightly and subsequently flattening out in the other. A similar 'virtual topography' effect on the phase of the flow response aloft was also noted by Armi & Mayr (2015) in their comparison of flow over the Sierras with the 1972 Boulder windstorm described by Lilly (1978).

Figure 8 shows snapshots of the inverse Richardson number $Ri^{-1} = (\partial v/\partial z)^2/N^2$ for the two cases, where N is the local, instantaneous stratification. Isopycnal overturns in the unstable downslope flow region are visible as patches of negative Ri^{-1}. In these simulations, we resolve the formation of the overturns, but the subsequent turbulent dissipation and mixing is modelled using a hyperdiffusive closure scheme. In the plunging interface case, sub-quarter Ri (i.e. $Ri^{-1} > 4$) occurs not only downstream, but also upstream and further aloft. As we will describe in § 6, the wave field aloft exhibits large fluctuations in the plunging interface case, suggesting the possibility of instability and nonlinear processes. By contrast, the upstream flow reaches steady state and remains stable despite Ri dropping below 1/4 in a thin region at the base of the flowing layer.

The emergent picture then is of an intrinsic dynamical connection between hydraulic control of the overflowing layer in direct contact with the topography and the wave field further aloft. The latter is essentially a response to the shape of the virtual topography formed by the top of the density interface and depends sensitively on the dynamics of the hydraulic flow component.

4. Theoretical framework – crest control and upstream subcriticality

The underlying basis of the framework we describe is hydraulic control, characterized by subcritical-to-supercritical flow transition at the obstacle crest. A flow profile is defined to be subcritical if it supports at least one long internal wave mode that is able to propagate upstream, supercritical if no such mode exists and critical if the

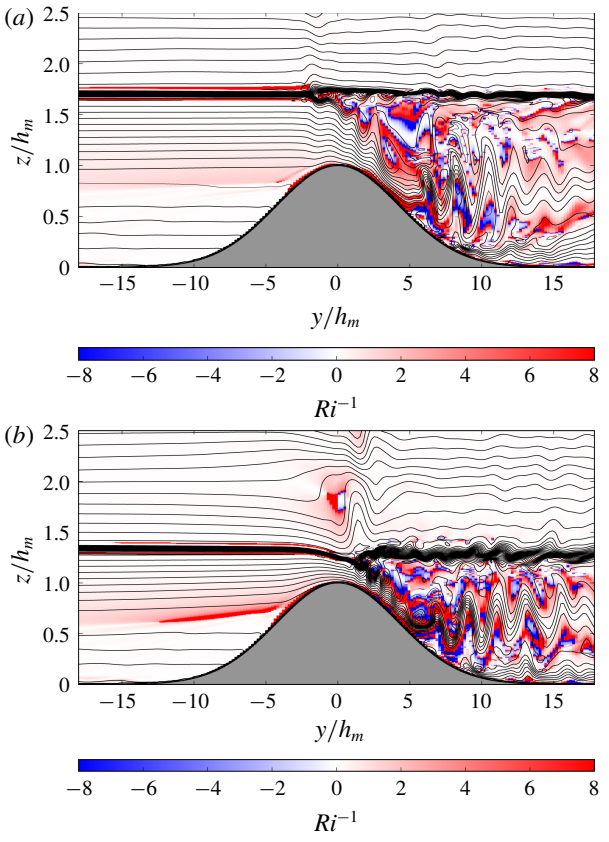

FIGURE 8. Instantaneous snapshots of the inverse Richardson number overlain with isopycnal contours. (*a*) Flat interface ($z_0 = 1.73h_m$) and (*b*) plunging interface ($z_0 = 1.33h_m$).

fastest upstream mode is exactly arrested (cf. Pratt *et al.* 1999; Pratt & Whitehead 2007). In the present context, this implies that when the density interface does not plunge, the upstream flow with uniform stratification N_0 and semi-parabolic velocity profile with peak speed given by (3.6) must be subcritical.

To check for subcriticality, we take the bottom and top of the overflowing layer as rigid boundaries of a waveguide, and solve the Taylor–Goldstein equation to determine whether the predicted upstream flow supports at least one upstream propagating internal wave mode. Assuming a background velocity profile $\bar{V}(z)$, uniform stratification N_0 and a wave-like disturbance with stream function $\psi = \phi(z)\exp(\mathrm{i}l(y-ct))$, the Taylor–Goldstein equation for a vertical wave mode $\phi(z)$ with speed c is

$$\frac{\mathrm{d}^2\phi}{\mathrm{d}z^2} - l^2\phi + \frac{N_0^2}{(\bar{V}(z)-c)^2}\phi - \frac{1}{(\bar{V}(z)-c)}\frac{\mathrm{d}^2\bar{V}(z)}{\mathrm{d}z^2}\phi = 0, \tag{4.1}$$

where $u = \mathrm{d}\psi/\mathrm{d}z$ and $w = -\mathrm{d}\psi/\mathrm{d}y$.

For the purpose of this analysis, we redefine the vertical coordinate z so that $z = 0$ is the bottom of the overflowing layer. The predicted upstream flow profile has

a semi-parabolic velocity distribution

$$\bar{V}(z) = 4v_m \left(\frac{z}{2\widetilde{H}} - \frac{z^2}{4\widetilde{H}^2} \right). \tag{4.2}$$

Bell (1974) showed that in a stratified flow with a sheared velocity profile $\bar{V}(z)$ and stratification $N(z)$ where the Richardson number Ri is greater than $1/4$ everywhere, internal wave modes come in pairs with speeds c_j^+ and c_j^- such that $c_j^+ > \max(\bar{V}(z))$ and $c_j^- < \min(\bar{V}(z))$. For $\bar{V}(z)$ given by (4.2), since $\bar{V}(0) = 0$, this implies that there always exists an upstream propagating mode provided $Ri > 1/4$ everywhere. However, as shown in figure 8(*b*) for the plunging interface case, Ri drops to sub-quarter values at the base of the flowing layer upstream and so the Taylor–Goldstein equation must be solved to conclusively determine subcriticality.

For the semi-parabolic velocity profile given by (4.2), equation (4.1) can be written as

$$\frac{\mathrm{d}^2\phi}{\mathrm{d}z^2} - l^2\phi + \frac{N_0^2}{v_m^2\left[4\left(\dfrac{z}{2\widetilde{H}} - \dfrac{z^2}{4\widetilde{H}^2}\right) - \dfrac{c}{v_m}\right]^2}\phi + \frac{2}{\widetilde{H}^2\left[4\left(\dfrac{z}{2\widetilde{H}} - \dfrac{z^2}{4\widetilde{H}^2}\right) - \dfrac{c}{v_m}\right]}\phi = 0, \tag{4.3}$$

with boundary conditions $\phi = 0$ at $z = 0, \widetilde{H}$. We now non-dimensionalize z as

$$\widehat{z} = z/\widetilde{H} \tag{4.4}$$

and confine attention to the fastest, long internal wave modes with $l \to 0$ that diagnose the criticality of the flow. Equation (4.3) then becomes

$$\frac{1}{\widetilde{H}^2}\frac{\mathrm{d}^2\phi}{\mathrm{d}\widehat{z}^2} + \frac{N_0^2}{v_m^2\left[4\left(\dfrac{\widehat{z}}{2} - \dfrac{\widehat{z}^2}{4}\right) - \dfrac{c}{v_m}\right]^2}\phi + \frac{2}{\widetilde{H}^2\left[4\left(\dfrac{\widehat{z}}{2} - \dfrac{\widehat{z}^2}{4}\right) - \dfrac{c}{v_m}\right]}\phi = 0, \tag{4.5}$$

with the boundary conditions $\phi = 0$ at $\widehat{z} = 0,\ 1$. Strictly speaking, while the base of the flowing layer intersects the topography and may thus be treated as a rigid boundary, the upper boundary is not a true rigid surface, but rather a pliant boundary that can move with the wave. When the fluid overlying the waveguide is stagnant and homogeneous, it is straightforward to impose matching pliant conditions at this boundary (e.g. Smith 1991). This is because the solution of (4.1) within the stagnant, homogeneous region takes a particularly simple form of exponential decay. In the flows considered here, the fluid overlying the upstream flowing layer is also stratified, so the formulation of a pliant boundary condition is less obvious. Here we have assumed simple rigid lid conditions at both vertical boundaries.

We now show that the criticality of the flow is completely determined by the two non-dimensional parameters Fr and the ratio z_0/h_m. First, we claim that for any $\gamma > 0$, equation (4.5) is invariant to the following transformation:

$$h_m \to \gamma h_m, \quad z_0 \to \gamma z_0, \quad N_0 \to N_0/\gamma. \tag{4.6a–c}$$

To see this, note that the transformation keeps the control parameter Fr and ratio z_0/h_m fixed. From (3.5) and (3.6), this leads to a re-scaling of the thickness of the

z_0/h_m	$\min(c_j^-)/V_\infty$	
	Excluding density interface	Including density interface
1.73	-0.64	-0.91
1.63	-0.35	-0.63
1.53	-0.11	-0.36
1.43	-10^{-5}	-0.13
1.33	5.4×10^{-5}	-10^{-3}
1.23	7.5×10^{-4}	4×10^{-4}

TABLE 1. Speed of the fastest upstream propagating internal wave mode ($\min(c_j^-)/V_\infty$) within the waveguide formed by the semi-parabolic overflow for different locations of the density step at $Fr = 0.16$.

semi-parabolic overflow $\widetilde{H} \to \gamma \widetilde{H}$, while v_m stays the same. Substituting these re-scaled quantities in (4.5) leaves it unmodified, which shows that the subcritical or supercritical character of the flow is insensitive to this transformation. We remark that this invariance property of (4.5) will not hold but for the long wave approximation $l \to 0$ that causes the second term in (4.3) to drop out.

If instead, we make the transformation

$$h_m \to \gamma h_m; \quad z_0 \to \gamma z_0; \quad V_\infty \to \gamma V_\infty, \tag{4.7a–c}$$

then Fr and z_0/h_m are once again unchanged, but (4.5) now becomes

$$\frac{1}{\widetilde{H}^2}\frac{\mathrm{d}^2\phi}{\mathrm{d}\widehat{z}^2} + \frac{N_0^2}{v_m^2\left[4\left(\dfrac{\widehat{z}}{2} - \dfrac{\widehat{z}^2}{4}\right) - \dfrac{\widehat{c}}{v_m}\right]^2}\phi + \frac{2}{\widetilde{H}^2\left[4\left(\dfrac{\widehat{z}}{2} - \dfrac{\widehat{z}^2}{4}\right) - \dfrac{\widehat{c}}{v_m}\right]}\phi = 0, \tag{4.8}$$

where $\widehat{c} = c/\gamma$. In other words, the eigenvalues of the rescaled problem differ from those of the original one by a factor of γ. However, the crucial point is that (4.8) has a negative eigenvalue if and only if (4.5) has one.

Thus only changes to Fr and z_0/h_m can affect the criticality of the flow. It follows that, for a fixed Fr, the criticality of the flow can only be altered by varying z_0/h_m. Based on the results from our numerical simulations, we hypothesize that for a given small Fr, there exists $\alpha > 1$ and a corresponding $z_{critical} = \alpha h_m$ such that for $z_{critical} < z_0 < z_{op}$, the waveguide formed by the semi-parabolic flow profile is subcritical.

Table 1 presents the speed $\min(c_j^-)$ of the fastest upstream propagating internal wave mode within the waveguide formed by this predicted upstream flow for different values of z_0/h_m at $Fr = 0.16$. The wave speeds were computed using the pseudo-spectral generalized eigenvalue solver described in Jagannathan *et al.* (2017). The second and third columns list the wave speeds for a waveguide that excludes and contains the sharp density interface, respectively.

When the bottom $z = z_0$ of the interface is below $z = z_{op} = 1.84h_m$ but above a height $1.33h_m$ from the ground, the predicted semi-parabolic upstream flow is subcritical. For $z_0 = 1.73h_m$, table 1 shows that $\min(c_j^-) = -0.64V_\infty$. Thus the bifurcating isopycnal is predicted to lie at the base of the density step. This prediction is consistent with the asymmetric crest-controlled flow observed in the numerical simulation for this case (figure 4).

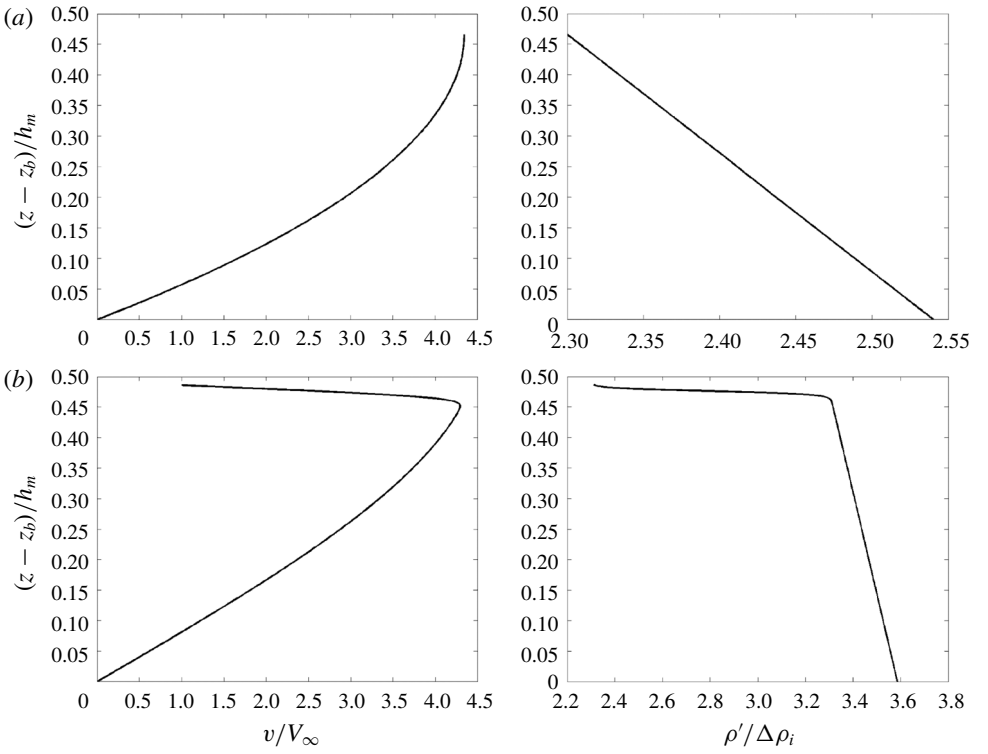

FIGURE 9. Prediction of vertical profiles of the velocity and density within the overflowing layer at the blocking location $y = -y_b$ for the case $z_0 = 1.33h_m$, with $N_{\delta_i}/N_0 = 8.6$. Note that the vertical coordinate z has been redefined so that $z = 0$ is the base of the flowing layer. Panel (*a*) excludes the density interface, whereas (*b*) includes the density interface.

At $1.33h_m$, which we identify as $z_{critical}$, this profile becomes supercritical, which is in violation of the hydraulic control assumption. To resolve this inconsistency, we first note that shifting the upper boundary of the waveguide to include the density interface will increase the mean stratification of the waveguide and thus allow faster upstream propagating waves. Therefore a plausible way to maintain subcriticality is to require that the density interface be part of the controlled overflow. That is, the isopycnal bifurcation occurs at the top rather than base of the density step. The third column of table 1 reveals that for $z = z_{critical}$, the upstream flow indeed becomes subcritical when the density interface is considered to be part of the waveguide. The flow profiles used in performing the wave speed computations for this case are shown in figure 9. The computed flow solution for this case (figure 6) corroborates the waveguide analysis, *viz.* the top of the density step plunges across the crest as part of the overflow.

When $z_0 < z_{critical}$, the semi-parabolic prediction fails to be subcritical even when the interface is considered to be part of the waveguide. Based on the low Ri values observed in figure 8(*b*) at the base of the flowing layer upstream, it is likely that $z_{critical}$ is near the margin of stability for the semi-parabolic flow configuration. Indeed, simulations for cases with $z_0 < z_{critical}$ indicate that, while the overflow continues to be asymmetric and hydraulically controlled, its shape and thickness progressively deviate from the predictions here as z_0 moves further and further below $z_{critical}$. The upstream

flow in these cases appears to maintain subcriticality through an upward shifting of the bifurcating isopycnal, to some intermediate height between $z_0 + \delta_i$ and z_{op}. That is, in addition to the density interface, a portion of the overlying fluid also plunges across the crest as part of the hydraulically controlled overflow.

5. Pressure drag

The pressure drag is a useful diagnostic to characterize the degree of cross-crest asymmetry in flow across topography. It is defined as the decelerating force exerted on the flow by the obstacle,

$$F_D = \int_{-\infty}^{\infty}\int_{-\infty}^{\infty} p_s \frac{\partial h}{\partial y}\,\mathrm{d}y\,\mathrm{d}x = \int_{-\infty}^{\infty}\int_{-\infty}^{\infty} h\frac{\partial p_s}{\partial y}\,\mathrm{d}y\,\mathrm{d}x, \tag{5.1}$$

where p_s is the pressure on the obstacle surface. The dynamical significance of pressure drag is that it removes horizontal momentum from the large scale flow and must thus be parameterized in general circulation models of the ocean and atmosphere which do not resolve flow details in the vicinity of topography. For a 2-D obstacle, it is appropriate to consider the drag force per unit length:

$$F_D = \int_{-\infty}^{\infty} p_s \frac{\partial h}{\partial y}\,\mathrm{d}y = \int_{-\infty}^{\infty} h\frac{\partial p_s}{\partial y}\,\mathrm{d}y. \tag{5.2}$$

As Winters & Armi (2014) show, in blocked downslope flows, there is a continuous drop in surface pressure starting at the upstream blocking location. It is this pressure drop that accelerates the lowest isopycnal of the overflowing layer up and across the crest. Consequently, there arise large surface pressure anomalies between the upstream and downstream sides, which will produce a high drag force on the obstacle. Figure 10 shows the evolution of the normalized drag per unit length as a function of non-dimensional time $t'_\delta = t/t_\delta$ for the flat and plunging interface simulations. Here $t_\delta = V_\infty/\sigma_{y_\delta}$ is a time scale for the development of the overflow (Jagannathan *et al.* 2019) and σ_{y_δ} is the half-width of the ridge at the blocking level. The drag has been normalized with the force produced due to a 2-D hydrostatic linear mountain wave excited by a ridge of identical shape and height, and for the same values of the outer flow parameters, $F_{DL} = \rho_0 V_\infty N_0 h_m^2$ (see appendix A).

Both the flat and plunging interface flows gradually evolve to a high-drag state. After $t'_\delta \approx 30$, the relative amplification of the drag in the flat interface simulation has a mean value of around 3.25. In the plunging interface flow, a further reduction of the surface hydrostatic pressure occurs along the lee slope and the non-dimensional drag reaches a value of approximately 3.75 at late times. In other words, the pressure drag is approximately 15 % higher when the interface plunges. It is pertinent to consider that in realistic low Fr geophysical flows, lateral flow splitting will often mitigate the surface pressure anomaly across the topography. To illustrate this, we have also shown in figure 10 (dotted lines) the drag for uniformly stratified flow past a long but finite ridge, with cross- to along-stream length ratio 30 at the same $Fr = 0.16$ – a flow that was investigated in Jagannathan *et al.* (2019). At early times, the non-dimensional drag across this ridge approaches 1.5, but over a longer time scale, it drops to around half the linear value, consistent with the fact that flow splitting is a low-drag process compared to mountain wave excitation.

Under the assumption that the drag is dominated by the blocked response, Klymak, Legg & Pinkel (2010) used a two and a half layer model to predict its value in 2-D

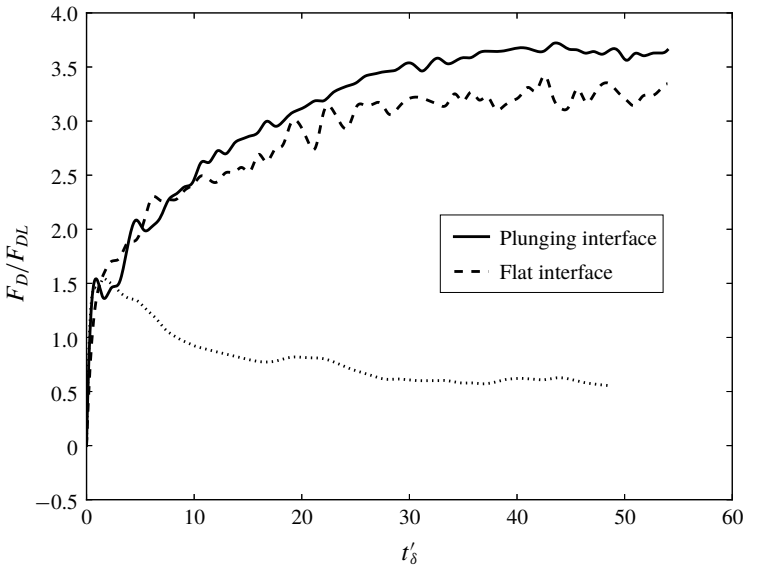

FIGURE 10. Evolution of the normalized pressure drag force. The dotted line represents the finite ridge case considered in Jagannathan *et al.* (2019) in which flow splitting leads to reduced drag.

flows where $Fr \ll 1$. When the total water depth $L_z \gg h_m$, this can be written in our notation as

$$F_{D_{2.5}} = \rho_0 V_\infty N_0 h_m^2 \frac{\pi}{2}(1 + \pi Fr - 2\pi^2 Fr^2). \tag{5.3}$$

From their 2-D simulations, Klymak *et al.* (2010) report that (5.3) approximates the drag quite well for very low values of Fr ($Fr \sim O(10^{-2})$). For the value $Fr = 0.16$ considered here (5.3) yields $F_{D_{2.5}} \approx 1.57\rho_0 V_\infty N_0 h_m^2$ which is an underprediction by a factor of 2 even in the 'flat-interface' case (figure 10). This is likely because (5.3) does not take into account the dynamics in the lee, in particular flow instabilities in the moderately low Fr flows considered here that lead to the formation of a deep, nearly stagnant and homogeneous isolating layer downstream (e.g. figure 4). The isolating layer causes a further drop in the lee surface pressure and thus an increase in the pressure drag.

6. The wave field aloft

A robust measure of the wave activity aloft is provided by considering the perturbation wave energy averaged over an appropriately defined area. The perturbation wave energy is the sum of its kinetic and potential energy contributions (KE and PE, respectively),

$$E(y, z, t) = \underbrace{\tfrac{1}{2}[(v - V_\infty)^2 + w^2]}_{KE} + \underbrace{\tfrac{1}{2}N^2\xi^2}_{PE}, \tag{6.1}$$

where $N(z)$ is the background stratification and $\xi(y, z, t)$ is the instantaneous isopycnal displacement at (y, z). For an obstacle with small aspect ratio $h_m/\sigma_y \ll 1$, the wave activity is largely confined to the region above the obstacle. We thus

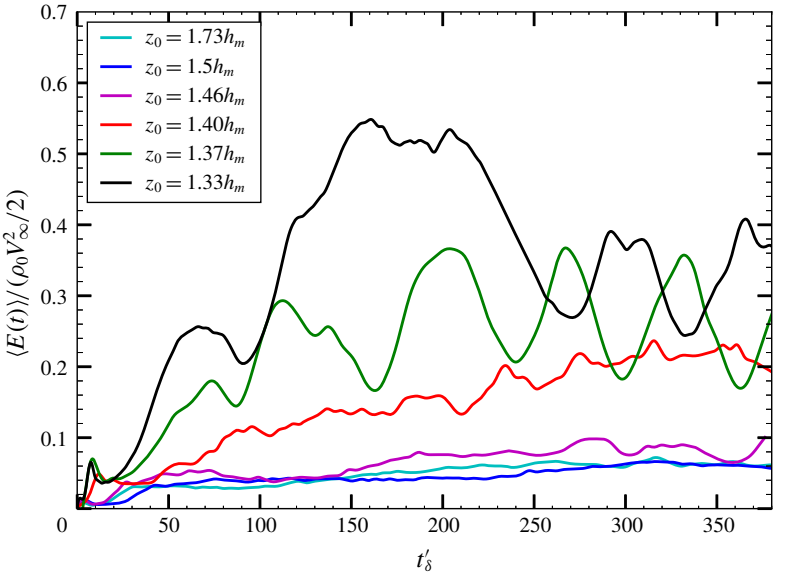

FIGURE 11. Evolution of the normalized wave energy density above the overflow, within the domain $(y, z) \in [-\sigma_y, \sigma_y] \times [2h_m, 4h_m]$.

define the wave energy density $\langle E(t)\rangle$ as the area average over the domain $(y, z) \in [-\sigma_y, \sigma_y] \times [2h_m, 4h_m]$. The normalized $\langle E(t)\rangle$ (figure 11) shows that at later times, the mean wave energy density in the plunging interface flow ($z_0 = 1.33h_m$) is over six times larger compared to the flat interface case ($z_0 = 1.73h_m$). Figure 11 also displays $\langle E(t)\rangle$ for simulations over a range of intermediate values of z_0/h_m. For $z_0/h_m > 1.4$, $\langle E(t)\rangle$ is found to be small, indicating that the interface remains mostly flat. In the range $1.4 \leqslant z_0/h_m < 1.33$, $\langle E(t)\rangle$ becomes oscillatory and its mean value grows steadily as z_0/h_m decreases towards 1.33. This suggests that the interface does not remain completely flat, rather a portion of it plunges. A complete dynamical description of these 'split interface' flows is beyond the scope of the present study.

There are large oscillations with time in the wave energy density when the interface plunges ($z_0 = 1.33h_m$), revealing a fluctuating nonlinear wave field aloft. This unsteadiness could be due partly to shear instability of the mean mountain wave solution itself, as suggested by the presence of a region aloft where *Ri* drops below 1/4 (figure 8*b*). In addition, perturbations at the top of the unstable plunging flow also propagate vertically and may interact with the mean mountain wave field. To further analyse the fluctuating wave field, we write the flow variables as the sum of time mean and eddy components,

$$u = V_\infty + \overline{u}(y, z) + u'(y, z, t), \tag{6.2a}$$
$$w = \overline{w}(y, z) + w'(y, z, t), \tag{6.2b}$$
$$p = p_0(z) + \overline{p}(y, z) + p'(y, z, t), \tag{6.2c}$$
$$b = b_0(z) + \overline{b}(y, z) + b'(y, z, t), \tag{6.2d}$$

where $b = -g\rho/\rho_0$ is the buoyancy and the steady background flow field is in hydrostatic balance $(1/\rho_0)\partial p_0/\partial z = b_0$. The sources of eddy kinetic energy (EKE)

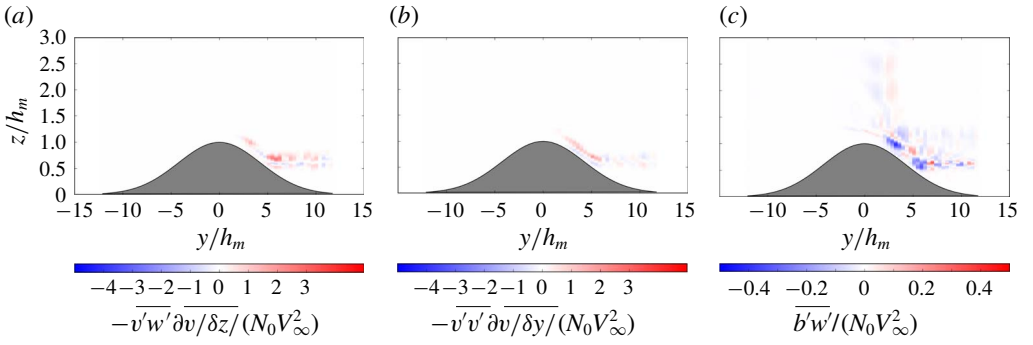

FIGURE 12. (Left to right) Normalized vertical Reynolds stress $VRS = -\overline{v'w'}\,\partial\overline{v}/\partial z$, horizontal Reynolds stress $HRS = -\overline{v'v'}\,\partial\overline{v}/\partial y$ and vertical buoyancy flux $VBF = \overline{b'w'}$ contributions to the EKE production for the plunging interface case ($z_0 = 1.33h_m$).

production in this flow are the vertical and horizontal Reynolds stress terms, $VRS = -\overline{v'w'}\,\partial\overline{v}/\partial z$, $HRS = -\overline{v'v'}\,\partial\overline{v}/\partial y$ and the vertical buoyancy flux $VBF = \overline{b'w'}$. The last term represents the reversible exchange of available potential energy between the mean and eddy flow fields.

The contributions of each of these terms to EKE production are displayed in figure 12 for the plunging interface case ($z_0 = 1.33h_m$). Time averages were taken over 50 snapshots, at a sampling rate of $0.5/t_\delta$. Downstream of the crest, *VRS* is of similar magnitude as *HRS* and both are an order of magnitude larger than *VBF*. This implicates the role of overturning Kelvin–Helmholtz instability (Jagannathan *et al.* 2017) in EKE production there. By contrast, further aloft *VBF* is the dominant term (figure 12*c*), suggesting that the unsteadiness aloft is a manifestation of continuous, reversible exchange of available potential energy between the mean and fluctuating wave fields.

The energy equation for internal waves can be written as (e.g. Gill 1982; Nash, Alford & Kunze 2005)

$$\frac{\partial E}{\partial t} + \boldsymbol{\nabla}\cdot(E\boldsymbol{u}) + \boldsymbol{\nabla}\cdot(p\boldsymbol{u}) = -\epsilon, \tag{6.3}$$

where $\boldsymbol{u}$ is the velocity vector, $\boldsymbol{\nabla}$ the gradient operator and ϵ the rate of energy dissipation, in this case, due to hyperviscosity.

We define integral, time mean energy fluxes

$$VEF = \langle\overline{Ew + pw}\rangle = \int_{-\sigma_y}^{\sigma_y} \overline{Ew + pw}\,\mathrm{d}y, \tag{6.4a}$$

$$HEF = \langle\overline{E(v - V_\infty) + p(v - V_\infty)}\rangle = \int_{2h_m}^{4h_m} \overline{E(v - V_\infty) + p(v - V_\infty)}\,\mathrm{d}z, \tag{6.4b}$$

to quantify wave energy propagation. Focussing on the vertical component *VEF*, it encompasses a pressure work term $\overline{pw}$ and nonlinear advection of wave energy $\overline{Ew}$. The pressure work term can be further decomposed into time-mean and eddy components as

$$\langle\overline{pw}\rangle = \langle\bar{p}\bar{w}\rangle + \langle\overline{p'w'}\rangle. \tag{6.5}$$

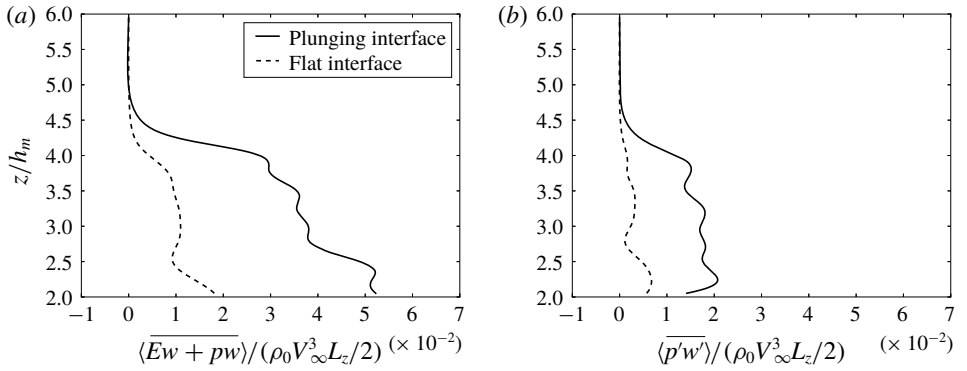

FIGURE 13. Vertical energy fluxes as defined in (6.5) for the flat ($z_0 = 1.73h_m$) and plunging ($z_0 = 1.33h_m$) interface cases: (*a*) total flux including nonlinear energy advection. (*b*) Eddy component due to the pressure work term.

For a linear mountain wave in an unbounded atmosphere, the direction of the group velocity is vertically upward and tilted upstream. The vertical energy flux then remains constant with height (Eliassen & Palm 1961), with nonlinear advection $\overline{Ew}$ being negligible. Figure 13(*a*) shows that between $z = 2h_m$ and $4h_m$, *VEF* is on average, approximately three times larger when the interface plunges. The pressure work $\overline{pw}$ and nonlinear advection $\overline{Ew}$ (not shown separately) are found to be of similar order and further, the wave energy flux also includes a significant eddy component (figure 13*b*). Horizontal flux and dissipative losses account for the net decrease in *VEF* between $z = 2h_m$ and $4h_m$. Interestingly, even in the case when the interface remains approximately flat and therefore only produces a weak wave response aloft, *VEF* and $\overline{p'w'}$ exhibit non-negligible divergences in the vertical, particularly between $z_0/h_m = 2$ and 2.5. These likely arise due to interactions between the mean wave field and time-dependent vertically propagating disturbances excited downstream of the bifurcation region where the flow is unstable. Above $z \approx 4h_m$, the waves are strongly damped due to the presence of the sponge layer.

6.1. *Scaling estimate for the mean wave field*

Finally, we note that the amplitude of the mean mountain wave field aloft can also be deduced using heuristic scaling arguments as follows. In the case of the non-plunging density interface, the only perturbation of the interface is a bump around the bifurcation region (figure 4*a*). The size of this bump can be estimated from energetics arguments (e.g. Sheppard 1956) by which the vertical displacement of isopycnals within the interfacial layer is approximately V_∞/N_{δ_i}. Therefore the flow aloft responds to a virtual topography of height V_∞/N_{δ_i}. The response is dominated by an arrested lee wave with group velocity directed upwards, vertical wavelength $2\pi V_\infty/N_0$ and perturbation flow speed $N_0(V_\infty/N_{\delta_i})$ (cf. Queney 1948; Baines 1998), which is small relative to V_∞ whenever $N_0/N_{\delta_i} \ll 1$. The observed perturbation amplitude in figure 5 of $0.15V_\infty$ agrees well with the prediction $V_\infty N_0/N_{\delta_i} \approx 0.12V_\infty$.

In the plunging interface case, the top of the density interface forms a virtual topography for the flow above. As seen in figures 11 and 13(*b*), the wave response in this case is highly nonlinear, but we assume that its vertical wavelength again scales

as $2\pi V_\infty/N_0$. Klymak *et al.* (2010) also find in their simulations of low *Fr* flows that this scaling works reasonably well for nonlinear lee waves. We noted in § 3.2 that the interface plunges a depth of approximately $1.4V_\infty/N_0$ from its quiescent position. Energetic considerations, however, cap the maximum vertical excursion of isopycnals above the plunging density step at V_∞/N_0, giving a flow speed perturbation of approximately $N_0(V_\infty/N_0) = V_\infty$. In other words, compared to the non-plunging case, the wave amplitude is larger by a factor of N_{δ_i}/N_0. This prediction is consistent with the result from the computed flow (figure 7) at the blocking location where the time-averaged perturbation speed amplitude is seen to be comparable to the background value V_∞.

7. Summary and conclusions

The presence of a density step in the stratification profile can have a profound effect on the dynamics of fluid flow over topography. In this study we have demonstrated that, in low *Fr* blocked flows, a sharp density step above crest level can set the height of the isopycnal bifurcation and thereby influence both the nature of the hydraulically controlled overflow as well as the flow response further aloft.

The observations of Armi & Mayr (2015) showed that when a neutrally stratified layer is capped by a temperature inversion, i.e. a stable density step, the flow aloft responds to the virtual topography formed by the inversion layer. They found that, depending on the ambient conditions, the overflow may be subcritical, supercritical or hydraulically controlled and asymmetric across the crest. The exact nature of the overflow and the corresponding shape of the inversion across the crest were then shown to be well described using single-layer reduced-gravity hydraulics.

Unlike the Armi & Mayr (2015) study and the earlier works of Vosper (2004) and Jiang (2014), in the present study, we consider a lower layer which is sufficiently stratified for blocking effects to be significant. In these flows, the natural across-crest asymmetry induced by upstream blocking triggers a hydraulic response, regardless of the location of the step. This differs from the study of Vosper (2004) in which the formation of a hydraulic plunging flow depends sensitively on the inversion strength and location. The reduced gravity shallow water theory of Jiang (2014) is also rendered inapplicable when upstream blocking occurs. On the other hand, the hydraulic framework outlined here can successfully interpret the nature of the crest-controlled overflow and in particular predict whether the density interface will plunge across the crest. We find that a plunging density interface can give rise to a wave field aloft that is as much as six times more energetic and produces 15 % higher pressure drag compared to a non-plunging interface. In general the relative amplification of the wave energy density and drag will depend on the ratio N_{δ_i}/N_0.

In uniformly stratified, blocked, topographically controlled flows that feature a sharp density step, a one-way decoupling exists in the sense that the hydraulically controlled flow in contact with the topography is isolated from the flow further aloft. The energetics of the wave field aloft, however, depend sensitively on the dynamics of the controlled flow component. The top of the density step constitutes a ‘virtual topography’ for the flow above and whether or not it participates in the overflow is shown to be directly connected to the fundamental condition of maintaining a subcritical flow upstream. A hydraulic waveguide analysis correctly diagnoses the shape of the density interface across the crest. When the interface plunges across the crest, it produces a highly energetic wave field aloft. By contrast, when the interface remains flat, wave excitation is strongly suppressed. In general, a quantification of

the topographically controlled flow component is essential to determine the shape of the virtual topography and hence to predict the characteristics of the flow response further aloft.

Acknowledgements

This work was supported by the National Science Foundation, grant AGS-1540585. We wish to thank the three anonymous referees for their constructive and insightful suggestions that helped expand the scope of the paper.

Declaration of interests

The authors report no conflict of interest.

Appendix A. Linear drag for flow across a Gaussian obstacle

In the linear, hydrostatic limit, the drag force per unit length across an obstacle of form $z = h(y)$ is given by (see, e.g. Baines (1998))

$$F_{DL} = \frac{\rho_0 N_0 V_\infty}{\pi} \int_0^\infty |\widehat{h}(k)|^2 k \, \mathrm{d}k, \tag{A 1}$$

where $\widehat{h}(k)$ is the Fourier transform of $h(y)$, defined as

$$\widehat{h}(k) = \int_{-\infty}^{\infty} h(y) \mathrm{e}^{-\mathrm{i}ky} \, \mathrm{d}y. \tag{A 2}$$

For a Gaussian-shaped ridge, $h(y) = h_m \mathrm{e}^{-y^2/\sigma_y^2}$, we have

$$\widehat{h}(k) = h_m \int_{-\infty}^{\infty} \mathrm{e}^{-y^2/\sigma_y^2} \mathrm{e}^{-\mathrm{i}ky} \, \mathrm{d}y. \tag{A 3}$$

This integral can be evaluated by standard methods. For example, taking the derivative with respect to k of (A 3):

$$\frac{\mathrm{d}\widehat{h}(k)}{\mathrm{d}k} = \mathrm{i}\frac{h_m \sigma_y^2}{2} \int_{-\infty}^{\infty} \frac{\mathrm{d}}{\mathrm{d}y}(\mathrm{e}^{-y^2/\sigma_y^2}) \mathrm{e}^{-\mathrm{i}ky} \, \mathrm{d}y. \tag{A 4}$$

After integration by parts and applying limits, this simplifies to the ordinary differential equation

$$\frac{\mathrm{d}\widehat{h}(k)}{\mathrm{d}k} = -\frac{\sigma_y^2 k}{2} \widehat{h}(k), \tag{A 5}$$

which has the solution

$$\widehat{h}(k) = C \mathrm{e}^{-\sigma_y^2 k^2/4}. \tag{A 6}$$

The unknown constant C is determined by evaluating the Fourier transform at $k = 0$:

$$C = \widehat{h}(0) = h_m \int_{-\infty}^{\infty} \mathrm{e}^{-y^2/\sigma_y^2} \, \mathrm{d}y = h_m \sigma_y \sqrt{\pi}. \tag{A 7}$$

Substituting (A 6) into (A 1) then gives the linear drag force per unit length as

$$F_{DL} = \rho_0 N_0 V_\infty \sigma_y^2 h_m^2 \int_0^\infty k \mathrm{e}^{-\sigma_y^2 k^2/2}\, \mathrm{d}k = \rho_0 N_0 V_\infty h_m^2. \tag{A 8}$$

REFERENCES

ARMI, L. & MAYR, G. J. 2015 Virtual and real topography for flows across mountain ranges. *J. Appl. Meteorol. Climatol.* **54** (4), 723–731.

BAINES, P. G. 1987 Upstream blocking and airflow over mountains. *Annu. Rev. Fluid Mech.* **19** (1), 75–95.

BAINES, P. G. 1998 *Topographic Effects in Stratified Flows*. Cambridge University Press.

BAINES, P. G. & HOINKA, K. P. 1985 Stratified flow over two-dimensional topography in fluid of infinite depth: a laboratory simulation. *J. Atmos. Sci.* **42** (15), 1614–1630.

BELL, T. H. 1974 Effects of shear on the properties of internal gravity wave modes. *Dtsch. Hydrogr. Z.* **27** (2), 57–62.

BRIGHTON, P. W. M. 1978 Strongly stratified flow past three-dimensional obstacles. *Q. J. R. Meteorol. Soc.* **104** (440), 289–307.

ELIASSEN, A. & PALM, E. 1961 On the transfer of energy in stationary mountain waves. *Geophys. Publ.* **22**, 1–23.

EPIFANIO, C. C. & DURRAN, D. R. 2001 Three-dimensional effects in high-drag-state flows over long ridges. *J. Atmos. Sci.* **58** (9), 1051–1065.

GILL, A. E. 1982 *Atmosphere-Ocean Dynamics*. Academic press.

HUNT, J. C. R., FENG, Y., LINDEN, P. F., GREENSLANDE, M. D. & MOBBS, S. D. 1997 Low-Froude-number stable flows past mountains. *Il Nuovo Cimento C* **20** (3), 261–272.

JAGANNATHAN, A., WINTERS, K. B. & ARMI, L. 2017 Stability of stratified downslope flows with an overlying stagnant isolating layer. *J. Fluid Mech.* **810**, 392–411.

JAGANNATHAN, A., WINTERS, K. B. & ARMI, L. 2019 Stratified flows over and around long dynamically tall mountain ridges. *J. Atmos. Sci.* **76** (5), 1265–1287.

JIANG, Q. 2014 Applicability of reduced-gravity shallow-water theory to atmospheric flow over topography. *J. Atmos. Sci.* **71** (4), 1460–1479.

KLYMAK, J., LEGG, S. & PINKEL, R. 2010 High-mode stationary waves in stratified flow over large obstacles. *J. Fluid Mech.* **644**, 321–336.

LEGG, S. & KLYMAK, J. 2008 Internal hydraulic jumps and overturning generated by tidal flow over a tall steep ridge. *J. Phys. Oceanogr.* **38** (9), 1949–1964.

LILLY, D. K. 1978 A severe downslope windstorm and aircraft turbulence event induced by a mountain wave. *J. Atmos. Sci.* **35** (1), 59–77.

LONG, R. R. 1955 Some aspects of the flow of stratified fluids. III. Continuous density gradients. *Tellus* **7**, 341.

MILES, J. W. & HUPPERT, H. E. 1969 Lee waves in a stratified flow. Part 4. Perturbation approximations. *J. Fluid Mech.* **35** (3), 497–525.

NASH, J. D., ALFORD, M. H. & KUNZE, E. 2005 Estimating internal wave energy fluxes in the ocean. *J. Atmos. Ocean. Technol.* **22** (10), 1551–1570.

PAL, A., SARKAR, S., POSA, A. & BALARAS, E. 2017 Direct numerical simulation of stratified flow past a sphere at a subcritical Reynolds number of 3700 and moderate Froude number. *J. Fluid Mech.* **826**, 5–31.

PELTIER, W. R. & SCINOCCA, J. F. 1990 The origin of severe downslope windstorm pulsations. *J. Atmos. Sci.* **47** (24), 2853–2870.

PIERREHUMBERT, R. T. & WYMAN, B. 1985 Upstream effects of mesoscale mountains. *J. Atmos. Sci.* **42** (10), 977–1003.

PRATT, L. J., JOHNS, W., MURRAY, S. P. & KATSUMATA, K. 1999 Hydraulic interpretation of direct velocity measurements in the Bab al Mandab. *J. Phys. Oceanogr.* **29** (11), 2769–2784.

PRATT, L. J. & WHITEHEAD, J. A. 2007 *Rotating Hydraulics: Nonlinear Topographic Effects in the Ocean and Atmosphere,* vol. 36. Springer Science & Business Media.

QUENEY, P. 1948 The problem of air flow over mountains: a summary of theoretical studies. *Bull. Am. Meteorol. Soc.* **29**, 16–26.

SHEPPARD, P. A. 1956 Airflow over mountains. *Q. J. R. Meteorol. Soc.* **82** (354), 528–529.

SMITH, R. B. 1985 On severe downslope winds. *J. Atmos. Sci.* **42** (23), 2597–2603.

SMITH, R. B. 1991 Kelvin–Helmholtz instability in severe downslope wind flow. *J. Atmos. Sci.* **48** (10), 1319–1324.

SMOLARKIEWICZ, P. K. & ROTUNNO, R. 1989 Low Froude number flow past three-dimensional obstacles. Part I: baroclinically generated lee vortices. *J. Atmos. Sci.* **46** (8), 1154–1164.

TESSLER, Z. D., GORDON, A. L., PRATT, L. J. & SPRINTALL, J. 2010 Transport and dynamics of the Panay Sill overflow in the Philippine seas. *J. Phys. Oceanogr.* **40** (12), 2679–2695.

VOSPER, S. B. 2004 Inversion effects on mountain lee waves. *Q. J. R. Meteorol. Soc.* **130** (600), 1723–1748.

WINTERS, K. B. 2016 The turbulent transition of a supercritical downslope flow: sensitivity to downstream conditions. *J. Fluid Mech.* **792**, 997–1012.

WINTERS, K. B. & ARMI, L. 2012 Hydraulic control of continuously stratified flow over an obstacle. *J. Fluid Mech.* **700**, 502–513.

WINTERS, K. B. & ARMI, L. 2014 Topographic control of stratified flows: upstream jets, blocking and isolating layers. *J. Fluid Mech.* **753**, 80–103.

WINTERS, K. B. & DE LA FUENTE, A. 2012 Modelling rotating stratified flows at laboratory-scale using spectrally-based DNS. *Ocean Model.* **49**, 47–59.